Research article

New evidence for the photocatalytic efficiency of natural raw vermiculites to produce hydrogen from aqueous methanol solution

Marta Valášková [a,*], Miroslava Filip Edelmannová [a], Martin Reli [a], Michal Ritz [b], Alexandr Martaus [a], Eva Plevová [c], Kamila Kočí [a]

[a] VSB – Technical University of Ostrava, CEET, IET, 17. listopadu 2172/15, Ostrava-Poruba, 708 00, Czech Republic
[b] VSB – Technical University of Ostrava, Faculty of Material Science and Technology, 17. listopadu 2172/15, Ostrava-Poruba, 708 00, Czech Republic
[c] Institute of Geonics of the Czech Academy of Sciences, Studentska 1768, 708 00, Ostrava, Czech Republic

A R T I C L E   I N F O

A B S T R A C T

The potential of vermiculites as environmentally friendly photocatalysts for hydrogen production and pollutant degradation was demonstrated by a photocatalytic test in an aqueous 50 % methanol solution (MeOH50). After 4 h of irradiation with the commercial TiO_2 Evonik P25 catalyst, the H_2 yield was of 656.9 ± 4.2 μmol/$g_{cat.}$ For vermiculites Vm1, Vm3, and Vm4, hydrogen yields were comparable ($H_2 = 420.6 \pm 5.8$ μmol/g_{cat}; $H_2 = 414.2 \pm 1.8$ μmol/g_{cat}, and 449.3 ± 1.8 μmol/g_{cat}, respectively) but were lower in the presence of vermiculite-chlorite intermediate Vm2 ($H_2 = 385.1 \pm 6.6$ μmol/g_{cat}). After the extended 24-h irradiation, hydrogen yield was promoted by the negative tetrahedral charge, while the positive octahedral charge inhibited the photocatalytic decomposition of the MeOH50 into hydrogen in favor of the formation of CO and CH_4 byproducts. The decrease in methanol yield in the MeOH50 was effectively assessed by the red shift of the C–O and C–H bands in the Raman spectrum, corresponding to the photocatalytic production of H_2.

1. Introduction

Manufacturing processes leading to methanol release contribute to atmospheric, soil, and groundwater pollution. Today, commercial methanol is produced mainly from fossil fuel-derived syngas, produced either through natural gas steam reforming or the gasification of coal. Many investigators consider methanol (MeOH) as a potential hydrogen source due to its gravimetric hydrogen content of 12.6 % and efficient conversion to H_2 and CO_2 as final products. Aqueous methanol can serve as a potential source for the amplification of transfer hydrogenation of clean fuel or indirectly as a hydrogen storage material [1–3]. Generally, the four different thermochemical processes, including methanol steam reforming, partial oxidation of methanol, autothermal reforming of methanol and methanol decomposition can utilize methanol to produce hydrogen [4]. Cost-effective photocatalysts with excellent activity and stability for environmental remediation, such as semiconductor photocatalysts, have attracted increasing interest in order to boost H_2 yields [5–7] and aid in water purification by degrading pollutants in aqueous solutions [8,9]. Materials such as iron supported on clay minerals, perovskites, carbon-based materials, zeolites and metal-organic frameworks dramatically increased catalytic degradation rates of contaminants due to enhanced electron transfer and good mechanical stability [10,11].

Vermiculite is a natural silicate clay mineral that is harmless to both health and the environment making it suitable for immobilizing photocatalytically active particles. The structure of vermiculite consists of a 2:1 layer with an interlayer space that appears in the X-ray diffraction patterns with basal space values from 1.0 to 1.5 nm, depending on the number of water molecules hydrating the cations within the interlayer space. Vermiculites have been found to be effective catalysts and photocatalysts for the degradation of organic compounds in electrochemical Fenton-based processes [12,13] and for degradation of antibiotics in aqueous solutions [14,15]. Additionally, as a natural mineral, vermiculite has shown the ability to split water through organic dyes under visible light [16]. The photocatalytic decomposition of methanol-water solution to yield hydrogen has been effectively achieved in the presence of iron(III) oxide (α-Fe_2O_3)/vermiculite composites [17,18], NiO(II)/vermiculite composites [19], and photocatalytic water splitting over the CeO_2/Fe_2O_3/vermiculite composites [20].

Raman spectroscopy can be applied to detect vibrational modes of molecules within crystal structure. However, the Raman spectra of vermiculites and other clay minerals present more challenges than IR spectra making them less commonly used in practice [21]. The main challenge is the weakness of Raman signal due to the fluorescence overlapping the significant part of clay mineral spectra. Correction of fluorescence often introduces very high level of spectral noise, complicating the identification of spectral band wavenumbers. Relatively complicated and ambiguous is also assignment of spectral bands in spectra of clay minerals. Despite these challenges, Raman spectroscopy has become an attractive method for the determination of compounds in aqueous solutions for *in-situ* measurements, in spite that the band intensities of the OH stretching vibrations are weaker in the Raman spectra than in the IR spectra [22,23]. Interactions between the water molecules and the organic phase result in substantial orientation of the weakly hydrogen-bonded water molecules in the interfacial region. The Raman spectra of methanol water solution shows two broad peaks at 3200 and 3400–3500 cm^{-1} (liquid-like peaks [24]), associated with OH stretches in more-ordered and less-ordered hydrogen-bonding structures. The hydrogen bond between methanol and water molecules has been investigated by molecular simulations [25,26] and various spectroscopy techniques [27–31]. The presence of water as the major source of H_2 has a significant impact on the photocatalytic activity of methanol-to-H_2 conversion. Diluted methanol aqueous solution (<20 %) exhibited shift of the proton source from methanol to water leading to a decreased of H_2 productivity on titanium dioxide (TiO_2) photocatalysts [32]. Competitive adsorption between water and methanol molecules on the surface of the photocatalyst surface limits the access of methanol to the photocatalyst. In addition, there was a high free energy barrier demonstrated for the desorption of liquid products from of the surface of the photocatalysts, which likely further hinders the role of water in an aqueous solution of methanol [31].

Heterogeneous photocatalysis is one of the most economical and ecofriendly methods for hydrogen production and wastewater treatment. In recent years, clay supported semiconductor photocatalysts have shown higher photocatalytic activity and recyclability than pure semiconductor nanomaterials. Nevertheless, these natural materials have been only sporadically used as standalone photocatalysts for environmental remediation and energy production. Recently, kaolinite, montmorillonite, illite, and attapulgite have been assessed for the photocatalytic degeneration of bromo phenol blue dye and phenol as water pollutants [33]. Vermiculites from the deposits around the world are still only sporadically studied for their photocatalytic properties.

The novelty of this work lies is providing evidence and comparative analysis of the photocatalytic properties of vermiculites from different deposits on degradation of an aqueous methanol solution and the production of hydrogen. Additionally, this study is the first one to employ Raman spectroscopy for evaluating changes not only in the structure of vermiculites but also in methanol water solution before and after the photocatalytic experiment.

2. Experimental

2.1. Materials and samples

Vermiculite (sample Vm1) and chlorite-vermiculite (sample Vm2) were personally selected from Letovice crystalline ultrabasic amphibolites and metagabros complex contact zones (Bohemia Massif, Czech Republic). The commercial vermiculite from the Paraiba region of Brazil (sample Vm3) and Palabora mine in South Africa (sample Vm4) were supplied by the company Grena Co. (Veselí nad Lužnicí, Czech Republic). Vermiculite from Brazil occurs within the ultramafic complex or carbonatites as a result of weathering and hydrothermal vermiculitization process [34]. Vermiculite in the Palabora occurring in phlogopite- and apatite-rich pyroxenites was documented in sequence of phlogopite → hydrobiotite → vermiculite mixed-layers on the oxidation and migration of the Fe^{2+} ions from octahedra to the tetrahedra [35].

2.2. Characterization techniques

Vermiculites were prepared to the particle size fraction less than 0.04 mm by milling (a vibratory mill VM4 OPS Přerov, Czech Republic) at 1500 rpm for 2.5 min and then sieving.

X-ray fluorescence (XRF) elemental analysis was obtained using a SPECTRO XEPOS energy dispersive (ED-XRF) spectrometer (Spectro Analytical Instruments, Kleve, Germany). Each sample (2 × 4 g) was mixed with wax (0.9 g) and pressed to the pellets at 10 tons for 30 s using a manual hydraulic press (BSL-2, Brio, Czech Republic). The amount of Fe(II) was determined by redox titration with the 0.1 M solution of potassium dichromate ($K_2Cr_2O_7$).

Atomic Absorption Spectroscopy (AAS) both Flame AAS and Furnace AAS, (ContrAA 700, Analytik Jena, Germany) were used for quantifying metals in water-methanol mixtures.

X-ray powder diffraction analyses were carried out on the X-ray diffractometer Rigaku SmartLab (RIGAKU Corporation, Tokyo, Japan). The XRD patterns were recorded in the 5°–80° 2θ range with a step size of 0.01° and speed 0.5 deg/min under CuKα radiation

at 40 kV and 40 mA with a detector D/teX Ultra 250 in symmetrical Bragg-Brentano diffraction geometry.

The nitrogen physisorption measurements of vermiculite samples Vm1 and Vm2 were performed using the 3Flex physisorption set-up (Micromeritics, USA). The specific surface area BET was evaluated according to the Brunauer–Emmett–Teller (BET) theory for the $p/p_0 = 0.05$–0.25.

Thermogravimetry and differential thermal analysis were carried out using the thermal analyzer Setsys 24 Evolution (Setaram, Caluire, France). The TG/DTA curves were obtained under following conditions: 25 mg of sample, final temperature 1000 °C, heating rate 10 K/min^{-1}, argon atmosphere, Al_2O_3 as reference material.

The UV–Vis diffuse reflectance spectra (UV–Vis DRS) were recorded using a Shimadzu UV-2600 Series spectrophotometer (Shimadzu Scientific Co., Tokyo, Japan) equipped with an external 2D detector in the wavelength range of 220–800 nm. Barium sulphate was a reference sample. Tauc curves were obtained using the Kubelka-Munk function to determine the direct band-gap energies (*Eg* in eV).

The photoluminescence (PL) spectra were obtained on the FLSP920 Series spectrometer (Edinburgh Instruments, Ltd.) in the wavelength range from 350 to 620 nm using Xe900 arc non ozone lamp 450 W (Steady State Lamp) and R928P type detector (PMT detector) and were measured with fixed excitation wavelength at 325 nm and the width of the excitation slit at 3.0 nm, emission slit at 3.0 nm and dwell time of 0.5 s.

Photoelectrochemical measurements were performed using photoelectric spectrometer and a three-electrode configuration, with Ag/AgCl and platinum wire as the reference and counter electrode, respectively. A thin layer of the analyzed material deposited on ITO-coated transparent PET foil (60 Ω/sq resistance, Sigma-Aldrich) served as working electrode. The electrolyte was purged by argon prior the photocurrent measurements for 15 min. Argon flow was kept constant during the whole experiment. Electrolyte was purged in order to remove oxygen. Photocurrents were recorded by irradiating the working electrode from the backside with a xenon lamp (150 W) in the range of 250–450 nm with 10 nm step (controlled by monochromator), applying voltages in the range between −0.2 and 1.0 V (vs Ag/AgCl). The size of the working electrode is determined by the diameter of the window (1.0 cm), so the area of the irradiated surface is 0.785 cm^2. Cyclic voltammetry scans were acquired in the dark after photocurrent measurements, with a 10 mV/s scan rate.

Photocatalytic decomposition tests were carried out in a home-made photoreactor (stainless steel, volume 305 ml). The reaction
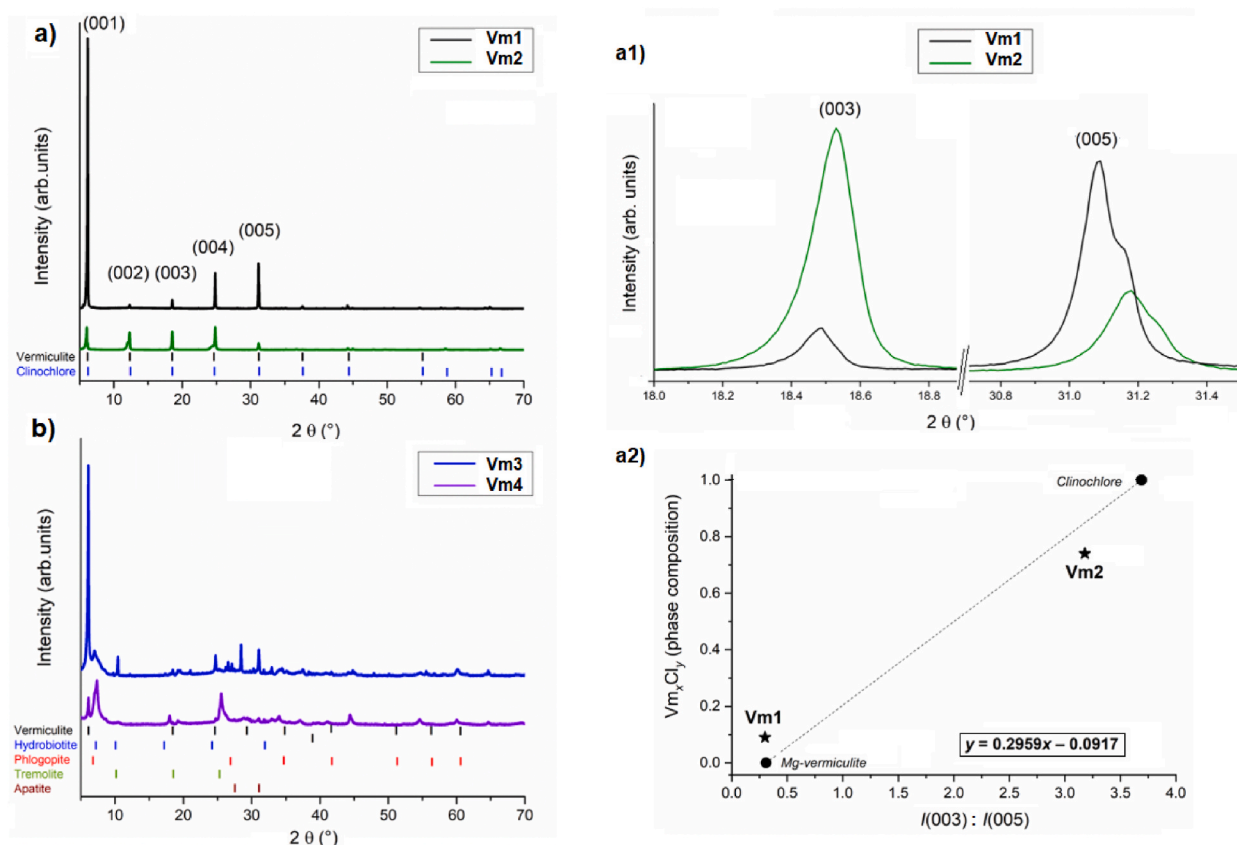

Fig. 1. XRD patterns of vermiculites: a) Vm1 and Vm2 and b) Vm3 and Vm4 from 5 to 70° 2 θ; a1) Vm1 and Vm2 with (003) and (005) basal diffractions; a2) the relation between intensities ratios *I*(003)/*I*(005) of Mg-vermiculite (Vm) and clinochlore (Cl) endmembers and calculated bi-phase composition of Vm$_x$Cl$_y$ in Vm1 and Vm2.

mixture, water-methanol (100 ml of 50 % methanol) with the photocatalyst (0.1 g), was bubbled with helium to remove oxygen and air from the photoreactor. The prepared reaction mixture was irradiated with an 8W Hg lamp (λ = 254 nm) (Ultra-Violet Products Inc., Upland, CA, USA), and gaseous samples were taken at regular intervals for 4 h. The gaseous products were analyzed using a gas chromatograph (Shimadzu Tracera GC-2010Plus, Shimadzu, Kyoto, Japan) equipped with a BID (barrier discharge ionization detector). All experiments (labelled Vm) were repeated at least three times (Fig. S1).

Stability tests of the photocatalyst were also conducted. The reaction mixture with the photocatalyst was irradiated for 24 h, after which the UV lamp was turned off, and the reaction mixture (with the same photocatalyst batch) was purged with helium to remove not only air but also any possible product of photocatalytic decomposition formed during the 24h irradiation. After the purge, the reactor was sealed and irradiated with an 8W Hg lamp. Gaseous samples were taken at regular intervals for 4 h. All experiments (labelled Vm-24) were also repeated at least three times and compared to the Vm experiments.

Raman spectra of vermiculite samples before and after photocatalytic experiment were measured on the dispersive Raman spectrometer DXR SmartRaman (ThermoScientific, Madison, WI, USA) with CCD detector using a backscattering configuration; the wavelength of excitation laser was 780 nm. Raman spectra were obtained at the spectral region 1000–50 cm^{-1}, using the grating 400 lines/mm, 50 μm slit aperture, laser power 20 mW, exposure time 1 s, and number of exposures 300.

Raman spectra of methanol water solution after the 24-h photocatalytic experiment were measured on the same instrument with the excitation laser wavelength at 532 nm. Raman spectra were obtained at the spectral region 4000–50 cm^{-1} using the grating 400 lines/mm, 50 μm slit, laser power 8 mW, exposure time 1 s, and number of exposures 200. The background measurement (for both Raman measurement) was performed on an empty sample compartment. The Raman spectra were treated (including fluorescence correction) by spectral software OMNIC (v.9.2; Thermo Scientific, Madison, WI, USA).

3. Results and discussion

3.1. Chemistry and mineralogy of vermiculites

X-ray diffraction was employed to identify the crystalline phases and detect any structural changes. Vermiculites from different geological locations differ mainly in the chemical composition of the interlayer space, which is characteristic of the mineral phases diffracting on the XRD patterns (Fig. 1). The layer sequences of Vm1 and Vm2 correspond to vermiculite (Vm, PDF card No.01-076-0847) and clinochlore (Cl, PDF card No.01-087-2496) (Fig. 1a), respectively. Vermiculites Vm3 and Vm4 (Fig. 1b) are mixed layer structures composed of the randomly stacked layers of vermiculite (Vm, PDF card no. 00-076-0847), hydrobiotite (Hb, PDF card No.00-049-1057) and phlogopite (Ph, PDF card No.01-074-3145). The different basal space value from 1.0 nm (in Ph) to 1.5 nm (in Vm) is related to the number of water molecules hydrating cations in the interlayer space. Vermiculite Vm3 is composed of Vm, prevailing slightly over Hb and Ph. The accessory minerals from the parent rocks were tremolite (PDF card no. 00-009-0437). In Vm4 prevails Hb over Vm and a minority of Ph. Hydroxyapatite (JCPDS card no. 00-064-0738) as an accessory mineral originated from the parent rocks.

The basal peaks positions of chlorite and vermiculite in Vm1 and Vm2 are very similar and only distribution of intensities is different. Vm2 produced on XRD pattern vermiculite-chlorite intermediate structure [36] characteristic with the overlap of the basal diffractions of the vermiculite and chlorite manifested itself in their asymmetric profile. The most significantly different intensities of basal (003) and (005) diffractions between the vermiculite and chlorite (Fig. 1a1) were selected for the relationship between the Mg-vermiculite and clinochlore endmembers using the intensity ratio $I(003)/I(005)$ of the Mg-vermiculite (Vm, PDF card no. 01-076-0847) = 0.31 and clinochlore (Cl, PDF card no. 01-087-2496) = 3.69. The linear relation can be written using the equation Eq (1), allowing to calculate chlorite (Cl) proportion in the chlorite-vermiculite intermediate layer structure.

$$y = 0.2959x - 0.0917 \tag{1}$$

where y is layer proportion of Cl calculated in Vm/Cl intermediate structure (Fig. 1a2).

Table 1
The structural formulas of the vermiculites.

Sample	Occupancy of cations			Layer charge $^{(-)}$
	Interlayer	Tetrahedral sheet $^{(-)}$	Octahedral sheet $^{(+)}$	
Vm1: $Mg_{0.33}Na_{0.01}$	$(Si_{2.77}Al_{1.23})^{-1.23}$	$(Mg_{2.42}Al_{0.17}Fe^{III}_{0.36}Fe^{II}_{0.03}Ti_{0.02})^{+0.57}O_{10}(OH)_2$		-0.66
Vm2:	$(Si_{3.60}Al_{0.40})^{-0.40}$	$(Mg_{4.64}Al_{0.55}Fe^{III}_{0.47}Fe^{II}_{0.01})^{+0.36}O_{10}(OH)_8$		-0.04
Vm3: $K_{0.18}Na_{0.08}Ca_{0.12}$	$(Si_{3.13}Al_{0.87})^{-0.87}$	$(Mg_{2.50}Fe^{III}_{0.36}Fe^{II}_{0.03}Al_{0.05}Ti_{0.04})^{+0.29}O_{10}(OH)_2$		-0.58
Vm4: $K_{0.33}Na_{0.02}Ca_{0.19}$	$(Si_{3.10}Al_{0.78}Fe^{III}_{0.12})^{-0.9}$	$(Mg_{2.51}Fe^{III}_{0.25}Fe^{II}_{0.08}Ti_{0.06})^{+0.17}O_{10}(OH)_2$		-0.73

The XRD patterns enable the calculation of intensity ratios $I(003)/I(005)$ yielding values of 0.30 for Vm1 and 3.18 for Vm2. According to Eq (1), Vm1 can be classified as vermiculite, while Vm2 corresponds to a chlorite-vermiculite layer structure with an intermediate $Cl_{0.85}Vm_{0.15}$ composition.

The structural formula of the trioctahedral vermiculites Vm1, Vm3, and Vm4 and chlorite Vm2 (Table 1) is another important mineral characteristic recalculated from elemental compositions determined by XRF analyses: (i) vermiculites were recalculated to their stoichiometric coefficients/$O_{10}(OH)_2$ in the four tetrahedral positions, the three octahedral positions and interlayer positions and (ii) chlorite was recalculated to the stoichiometric coefficients/$O_{10}(OH)_8$, while Mg was considered, in both the brucite sheet and in the interlayer space between the two 2:1 layers [37].

TG/DTA analysis provided additional information about the structural characteristics of vermiculites and chlorite-vermiculite intermediate structure (Fig. 2). The TG/DTA showed two sharp endothermic reactions at around 140 and 250 °C, possibly corresponding to the two stages of dehydration of the interlayer region of the vermiculite layer.

In the temperature range from 250 to 700 °C, a slight mass loss (approximately 1.5 wt%) was observed in Vm1, Vm3 and Vm4, corresponding to the dehydroxylation and/or the slow dehydration of water molecules tightly held in the interlayer. In Vm2, a significant endothermic peak at 621 °C was attributed to the dehydration of the Mg-OH bond in the "brucite" layer in magnesian chlorite [38]. The total mass loss from 25 to 700 °C was approximately 15.9 wt% for Vm1 and 11.2 wt% for Vm2, while for Vm3 and Vm4 it was about 7.7 and 5.5 wt%, respectively (Table 2). The XRD pattern of the crystalline products at 1000 °C (Fig. 3) allow to assume the formation of clinoenstatite ($MgSiO_3$, PDF card No. 00-019-0769) in Vm1 (TG exothermic peak at 861 °C), clinoenstatite and forsterite (Mg_2SiO_4, PDF card No. 01-085-1357) in Vm2 (TG exothermic peaks at 836 and 819 °C), phlogopite (PDF card 01-082-2699) and clinoenstatite in Vm3 (TG exothermic peaks at 858 °C) and phlogopite and forsterite in Vm4 (TG exothermic peaks at 843 °C).

3.2. UV–visible and photoluminescence spectra of vermiculites

Ultraviolet–visible (UV–Vis) and photoluminescence (PL) spectra of vermiculite samples were used to predict photochemical properties by estimating the band gap energy (Eg) and assessing photocatalytic activity through PL intensity (Fig. 4). The Eg represents the energy needed to excite an electron from the valence band to the conduction band, which is crucial for predicting photocatalytic properties of semiconductors [39].

The optical band gap energy (Eg) was obtained using the Tauc plot method [40] (Fig. 4b). This method assumes that the energy-dependent absorption coefficient α can be expressed by Equation (2).

$$(\alpha h\nu)^{1/\gamma} = A\left(h\nu - E_g\right) \tag{2}$$

where α is the absorption coefficient, h is the Planck's constant, ν is the photon's frequency, A is a constant, Eg is the band gap energy. The γ factor depends on the nature of electron transition and is equal to ½ or 2 for the direct and indirect transition band gaps, respectively.

Insertion of $F(R)$ instead of α yields the form according to Eq (3).

$$(F(R)\, h\nu)^{1/2} = A\left(h\nu - E_g\right) \tag{3}$$

where R is the reflectance $= R_{sample}/R_{standard}$

The reflectance from the UV–Vis diffuse-reflectance spectra (DRS) (Fig. 4a) can be recalculated to obtain absorption intensities. The x-axis of the Tauc plot gives an estimate of the band gap energy for the indirect transition using the Tauc coefficient $n = 2$ (Fig. 4b). As shown in Table 3, the Eg values 2.71 and 3.15 eV for Vm1, 2.75 and 3.21 eV for Vm3 and 3.26 eV for Vm4 were already reported for vermiculite [14]. The band gap energy 3.73 and 4.14 eV is indicative of a less efficient Vm2 semiconductor.

The photoluminescence (PL) signals of semiconductor materials result from the recombination of photo-induced charge carriers.
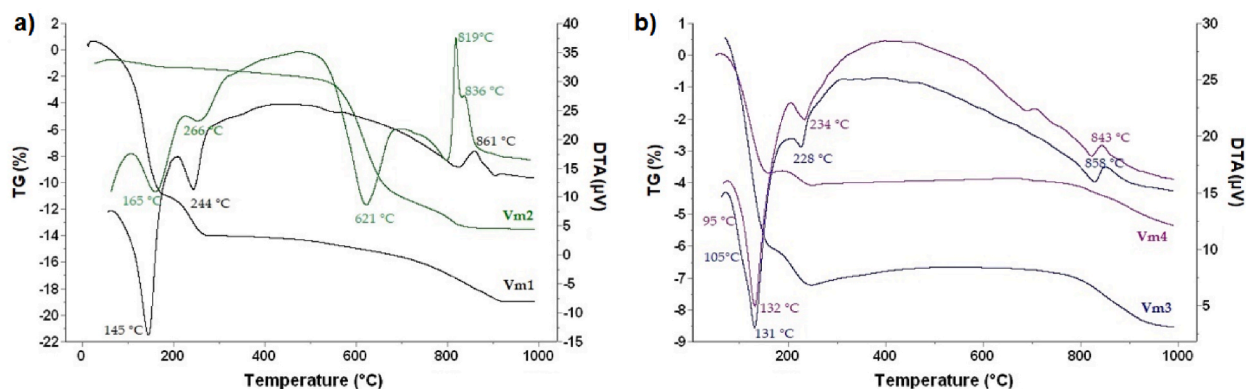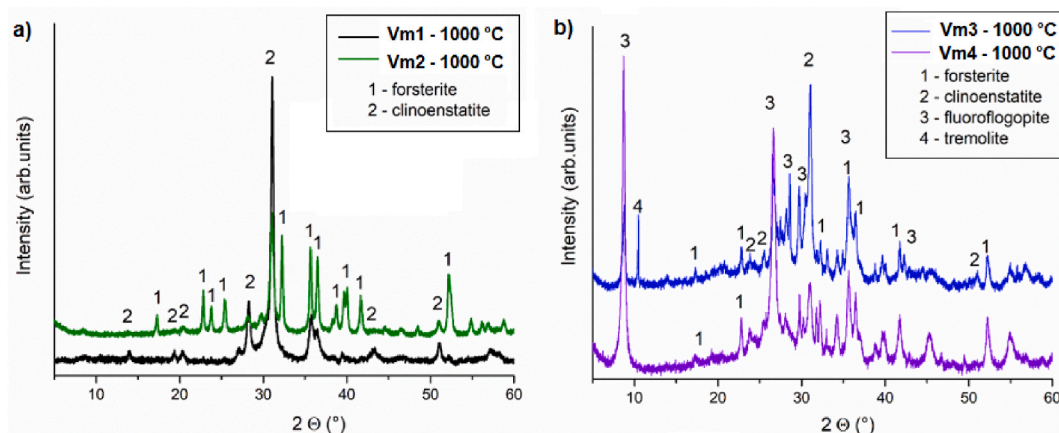

Fig. 2. The TG/DTA curves of the vermiculites: a) Vm1 and Vm2 and b) Vm3 and Vm4.

Table 2
Mass loss (Δm wt.%) in temperature intervals of dehydration and dehydroxylation processes.

Sample	Δm_1 (wt%) 20–170 °C	Δm_2 (wt%) 170–250 °C	Δm_3 (wt%) 250–700 °C	Total (wt%)
Vm1	−11.2	−3.1	−1.6	15.9
Vm2	−0.5	−1.0	−9.7	11.2
Vm3	−6.1	−1.1	−0.5	7.7
Vm4	−3.7	−0.4	−1.4	5.5

Fig. 3. The XRD patterns of vermiculites calcined at 1000 °C and mineral phases of: a) Vm1 and Vm2 and b) Vm3 and Vm4.

Generally, a lower PL intensity indicates slower recombination rate of photoinduced electron (e^-)–hole (h^+) pairs, which correlates with higher photocatalytic activity of semiconductor photocatalysts [41,42]. The low PL intensity of Vm1 and high PL intensity of Vm2 (Table 3, Fig. 4c) suggest their higher and lower photocatalytic activity, respectively. The bands in the PL spectra can be assigned as follows: the emission about 385 nm corresponds to the SiO_4^{4-} group in silicates, the subsequent emission bands around 450–490 nm correspond to the $Si^{IV}/(Al,Fe)^{III}$ substitution in tetrahedra (Table 1) and take place due to an electron-hole recombination at their $SiO_4^{4-}/Al,FeO_4^{5-}$ centers [43]. Emission bands at about 575 nm were assigned to the recombination of electrons trapped at oxygen vacancies near the conduction band edge with holes in deep Fe-related surface sites [44].

In order to explore the photogenerated electron transfer performance of vermiculite samples, the transient photocurrent responses were measured. The photocurrent action maps showing the dependence of photocurrent on wavelength and applied potential are given in Fig. 5.

Photocurrent measurements provide valuable insights into semiconductor properties. As expected, all vermiculite samples showed very similar and very low photocurrent responses. The low photocurrent was expected as vermiculites are natural minerals with low conductivity. It is clear vermiculites show only anodic photocurrent (red areas) which corresponds to the oxidation of an electron donor, mainly water in aqueous electrolyte. Anodic photocurrent is typical for p-type semiconductors, where the majority charge carriers are holes. Anodic photocurrent is favorable for methanol oxidation, since the reaction is initiated by hole.

Since the photocurrent responses are very similar and very low, the photocurrent generation at applied potential of 1 V is shown in Supplementary materials (Fig. S3). It is clear the responses are very low with a high level of noise. However, it can be clearly distinguished, that Vm4 sample generates higher photocurrent than the rest of the samples. Since the photocurrent is recorded at external potential of 1 V, the recombination of electrons and holes is significantly suppressed and higher photocurrent means higher amount of charge carriers generated after irradiation. PL spectra (Fig. 4c) suggest higher recombination rate for Vm4 sample compared to the Vm1 sample, however, based on the photocurrent measurement Vm4 sample generates more electrons and holes after irradiation. This is the reason, why Vm4 sample generates the highest hydrogen yield (Fig. 6) even though, its recombination rate of charge carriers is higher (Fig. 4). It simply generates more electrons and holes (Fig. S3).

3.3. Photocatalytic experiment with vermiculites in MeOH50

In the MeOH50-water solution, water competes with MeOH100 for valence band holes [45]. Water is being oxidized and splits into hydroxyl radicals (OH•) and H^+ ions. The hydroxyl radicals generate oxygen while H^+ ions form hydrogen. Electrons and holes are produced in equal amounts and can combine with electron acceptors such as H^+ in the solution, thereby reducing it to produce highly efficient and clean hydrocarbon [46]. The photon-generated holes act as oxidation sites for the adsorbed methanol molecules, as described by Eq (4) – Eq (7) below:
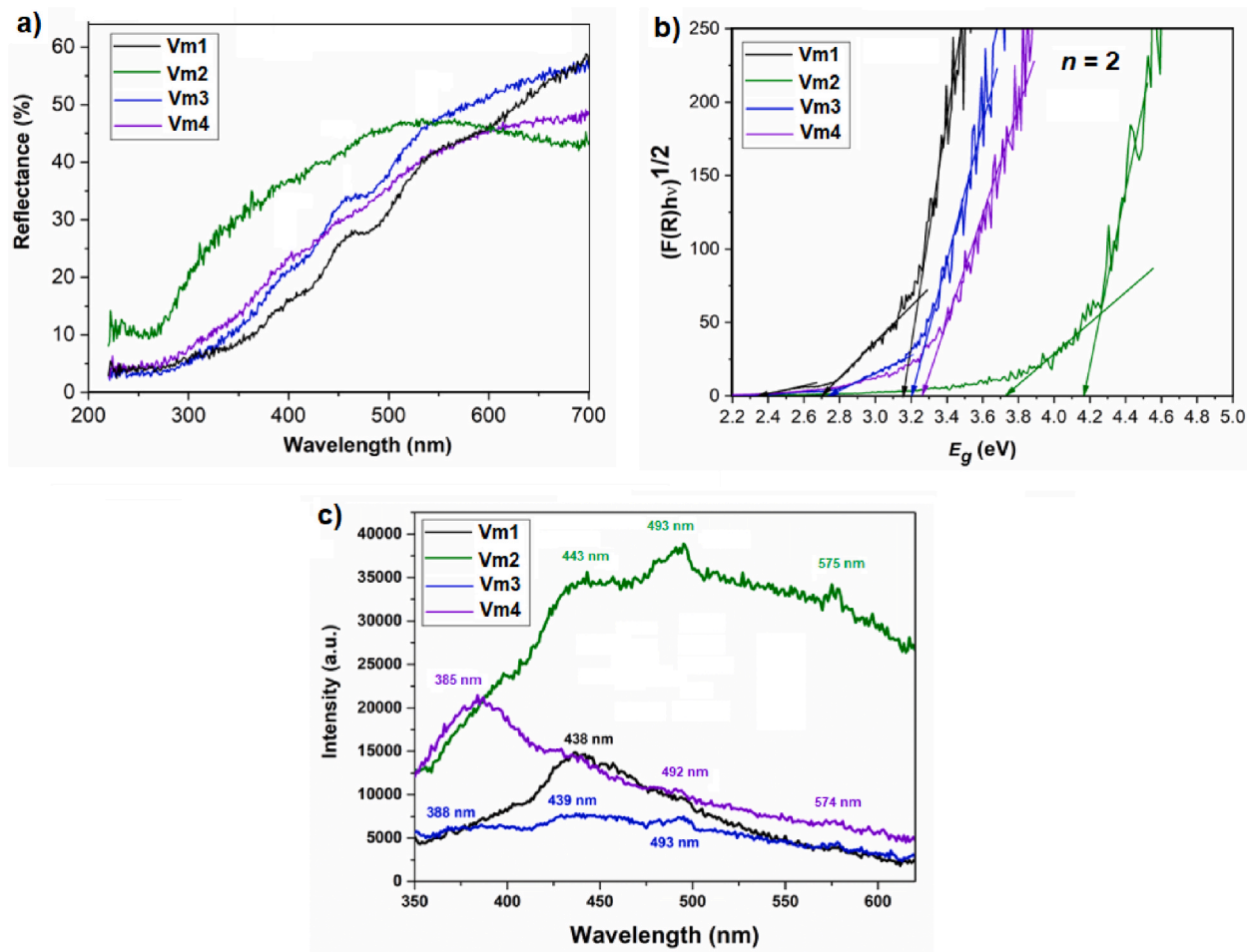
Fig. 4. UV–Vis and PL: a) DRS spectra, b) Tauc curves and c) PL spectra.

Table 3
The indirect Eg values band gap energies and maxima of emission peaks obtained from PL spectra.

Sample	E_g (eV)	PL (nm); (E_g in eV)
Vm1	2.35; 2.71; 3.15	438 (2.83)
Vm2	3.73; 4.17	443 (2.80); 493 (2.52); 575 (2.16)
Vm3	2.75; 3.21	388 (3.20); 439 (2.82); 493 (2.52); 575 (2.16)
Vm4	3.26	385 (3.22); 493 (2.52); 575 (2.16)

$$CH_3OH + h_{vb}^+ \rightarrow CH_3O^+H \tag{4}$$

$$CH_3O^+H \rightarrow CH_2O + H^\bullet + H^+ \tag{5}$$

$$H^+ + e_{eb}^- \rightarrow H^\bullet \tag{6}$$

$$H^\bullet + H^\bullet \rightarrow H_2 \tag{7}$$

Formaldehyde (CH_2O) in Eq (5) decomposes immediately by donating electron to the h_{vb} + forming carbon monoxide and additional hydrogen according to Eq (8):

$$CH_2O + h_{vb}^+ \rightarrow CO + H^+ + H^\bullet \tag{8}$$

The photocatalytic dissociation of methanol generates significant free radicals, which drive the mechanism responsible for the formation of methane (CH_4), Eq (9).
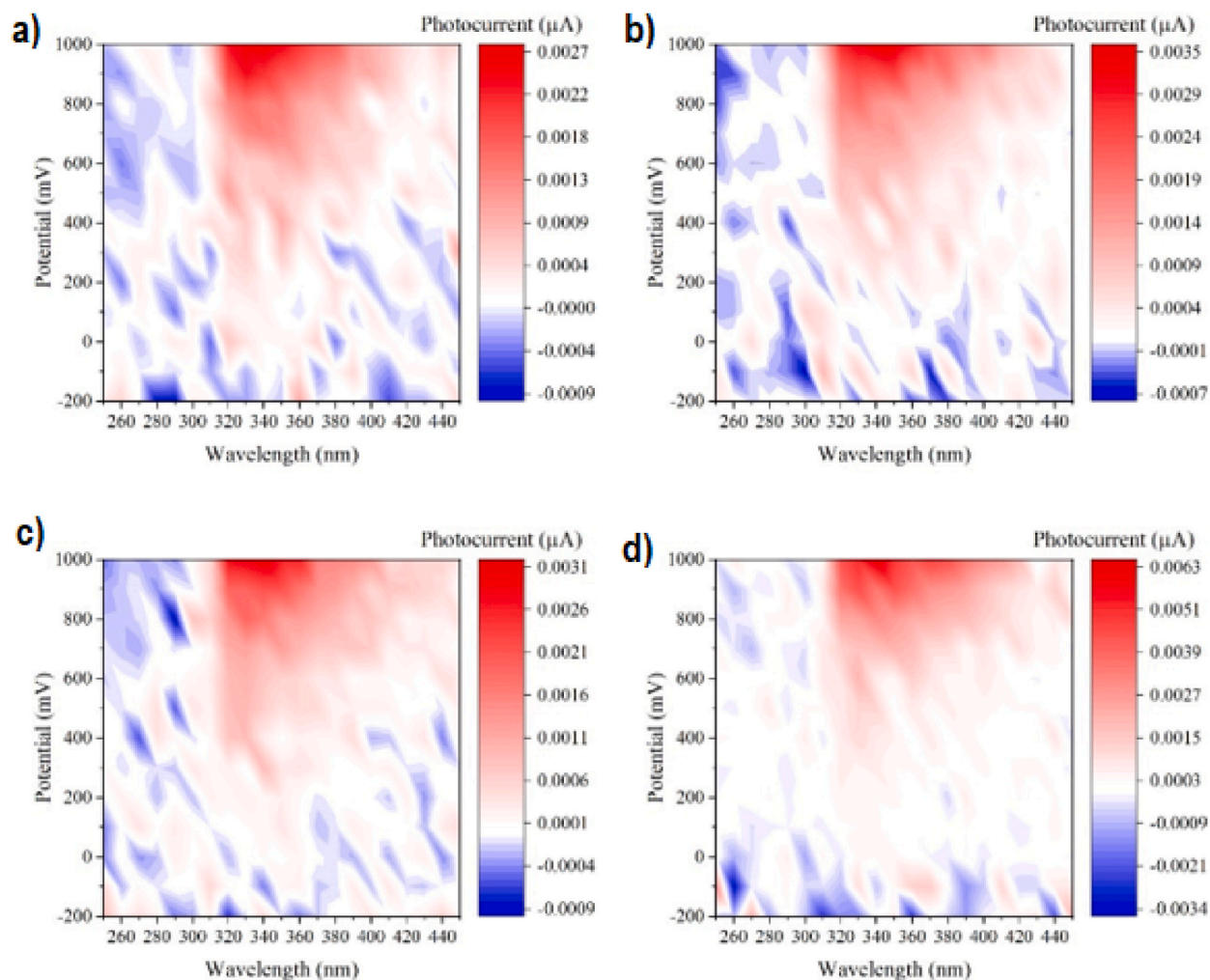
$$CH_3OH + H^\bullet \rightarrow CH_4 + HO^\bullet \tag{9}$$
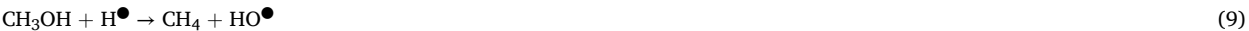
Fig. 5. Photocurrent action maps of a) Vm1; b) Vm2; c) Vm3; and d) Vm4.
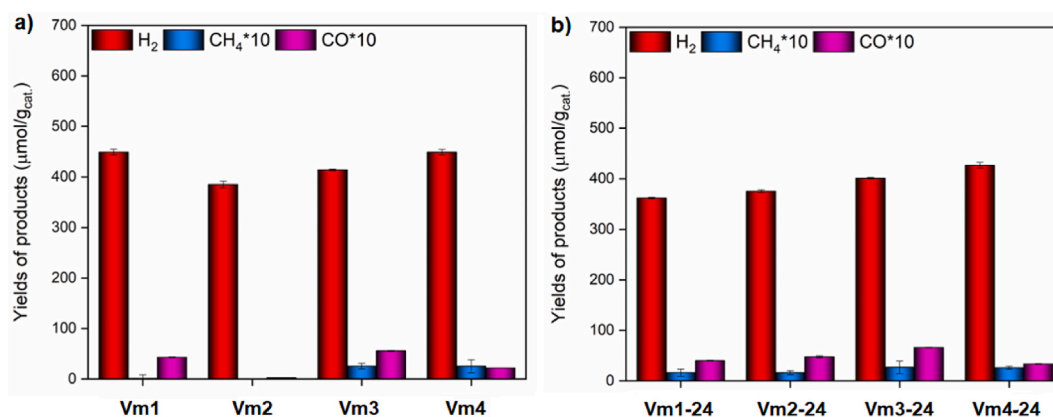

Fig. 6. Comparison of products from the photocatalytic decomposition of methanol after 4 h of irradiation in the presence of: a) Vm photocatalysts and b) Vm-24 photocatalysts. Yields of CH_4 and CO were multiplied by 10.

The band gap energy and PL spectra (Fig. 3) indicate that Vm1, Vm2, Vm3 and Vm4 are semiconductors with the expected photocatalytic efficiency on methanol-water degradation producing hydrogen and by-products CO and CH$_4$ (Fig. 6, Table 4). After 4 h of irradiation, Vm1 and Vm4 generated similar H$_2$ yields of 449.3 $\pm$ 1.8 µmol/g$_{cat.}$ and 449.1 $\pm$ 5.6 µmol/g$_{cat.}$, respectively, while H$_2$ yields in the presence of Vm3 and Vm2 were lower, 414.2 $\pm$ 1.8 µmol/g$_{cat.}$ and 385.1 $\pm$ 6.6 µmol/g$_{cat.}$, respectively, (Fig. 6a).

The H$_2$ yields in the presence of Vm1-24, Vm4-24, Vm3-24, and Vm2-24 after 4 h of irradiation were lower about 19.5, 5.0, 3.0 and 2.5 %, respectively, (Fig. 6b). The formation of CH$_4$ and CO by-products after 4 h of irradiation were also not the same. For comparison, in the presence of commercial TiO$_2$ Evonik P25 catalyst, the 4h-H$_2$ yield was of 656.9 $\pm$ 4.2 µmol/g$_{cat.}$ and in the presence of TiO$_2$ Evonik P25-24H$_2$ yield was 695.3 $\pm$ 2.1 µmol/g$_{cat}$; CO = 22.6 $\pm$ 1.9 µmol/g$_{cat.}$ and CH$_4$ = 0.3 $\pm$ 0.05 µmol/g$_{cat.}$ (not presented in Fig. 6). The rate constants of photocatalytic reaction were calculated and added to Table 4 and Figures to the Supplementary materials (Fig. S2).

It is generally accepted that the catalytic performance of clay mineral particles is associated with their total acidity due to terminal OH centers (Brønsted acids) and Al^{III}, Fe^{III} and Fe^{II} cations (Lewis acids) on both interlayer surfaces and edge surfaces [47].

The assumption that vermiculites absorbed 254 nm photons initiating the generation of valence band holes (h$^+_{vb}$) and conduction band electrons (e$^-_{eb}$) is supported by the production of hydrogen and small amounts of methane (CH$_4$) and carbon monoxide (CO) byproducts. In Fig. 7, a general scheme of the structure of vermiculites (Fig. 7a) carrying different negative tetrahedral charge and positive octahedral charge (Table 1) was related to the photocatalytic H$_2$ yields from methanol water solution after 4 h of irradiation in the presence of Vm and Vm-24 photocatalysts (Table 4). Fig. 7b shows that tetrahedra negative charge positively supported photocatalytic activity to hydrogen yield through both experimental times. However, the presence of Vm-24 tends to favor the formation of CO (Eq (8)) and CH$_4$ (Eq (9)) over H$_2$ production, likely due to the inhibitory effect of a higher positive charge on the octahedra sites.

The BET specific surface area of Vm1 = 10.7 m^2/g and Vm2 = 7.1 m^2/g and larger BET of Vm3 = 33.8 m^2/g and Vm4 = 42.6 m^2/g have positive impact on the photocatalytic decomposition of MeOH50. The stability of the photocatalysts surface was evaluated by the analysis of Na, Mg and Ca ions released from vermiculite's interlayer and octahedra to the methanol water solution (Table 5). Literature indicated that the mineral dissolution is a function of the number of reactive sites at the mineral/water interface, e.g., aluminol groups (Al-O-H) or silanol groups (Si-O-H). Macroscopic dissolution studies assumed that the BET surface area is identical with the reactive surface area. However, numerous examples evidenced no linear relationship between the BET surface area and the dissolution rate, indicating that the reactive surface area is not equivalent to the BET surface area [48].

3.4. Raman spectroscopic study

3.4.1. Raman spectra of vermiculites

The Raman spectral bands of vermiculites Vm1, Vm2, Vm3 and Vm4 from 800 cm^{-1} to 50 cm^{-1} (Fig. 8) and Vm1-24, Vm2-24, Vm3-24 and Vm4-24 after 24 + 4 h photocatalytic tests were assigned according to the previous Raman spectroscopy studies [21,38, 49–55] (Table 6).

Raman spectra of four vermiculite samples showed different intensities of spectral bands and different level of spectral noise (Fig. 8). The spectrum of Vm1 exhibited the lowest level of spectral noise. In comparison, the spectra of Vm2 and Vm3 showed higher noise level, although still allowing sufficiently accurate determination of the wavenumber of the observed spectral bands. However, the spectrum of Vm4 is too noisy for accurate determination of the wavenumbers of most spectral bands.

Raman spectra showed three intensive significant bands at about 680 cm^{-1}, 190 cm^{-1}, and 100 cm^{-1} in slightly shifted wavenumber positions. The band at about 680 cm^{-1} corresponds to the deformation vibration (E$_3$) of Mg-O in octahedra, appearing at 670 cm^{-1} for Vm1 and Vm3, at 675 cm^{-1} for Vm4, and 682 cm^{-1} for Vm2.

The band at about 190 cm^{-1} belongs to the deformation vibration of Mg-O-Mg in the octahedral sites of vermiculites. This band shifts to 191 cm^{-1} in Vm1 and Vm3, 196 cm^{-1} and 182 cm^{-1} in Vm2, and 183 cm^{-1} in Vm4 likely due to the different cations in octahedra (Table 1).

The band at about 100 cm^{-1} belongs to the vibration of interlayer cations in the interlayer space of vermiculite, as well as the movement of the octahedral sheet in chlorite.

Significant difference between the spectrum of sample Vm2 and spectrum of the rest of samples (Vm1, Vm3, and Vm4) is also in the intensity of spectra of the bands at about 190 cm^{-1} and 680 cm^{-1}. While intensities of spectra of samples Vm1, Vm3, and Vm4 are relatively similar, the spectrum of sample Vm2 is significantly weaker. The reason is likely due to greater layer disorder of the chlorite-

Table 4

The yields of H$_2$, CH$_4$ and CO obtained from photocatalytic decomposition of methanol water solutions in the presence of Vm and Vm-24 photocatalysts after 4 h of irradiation.

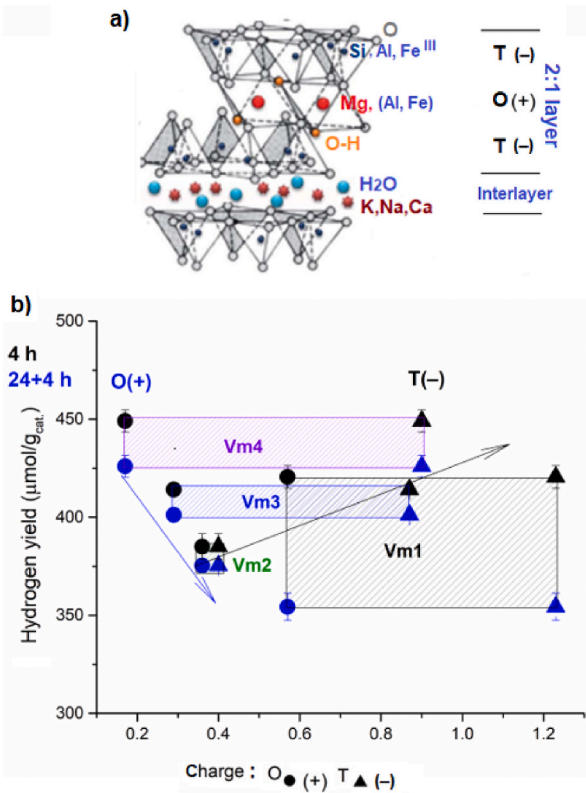| Sample	H$_2$ (µmol/g$_{cat.}$)	CH$_4$ (µmol/g$_{cat.}$)	CO (µmol/g$_{cat.}$)	kinetic constants (h^{-1})
Vm1	420.6 $\pm$ 5.8	0.14 $\pm$ 0.07	4.30 $\pm$ 0.10	104.2
Vm1-24	354.4 $\pm$ 4.9	1.64 $\pm$ 0.07	3.99 $\pm$ 0.10	64.4
Vm2	385.1 $\pm$ 6.6	0.03 $\pm$ 0.01	0.24 $\pm$ 0.01	94.7
Vm2-24	375.4 $\pm$ 2.7	1.62 $\pm$ 0.04	4.75 $\pm$ 0.20	90.9
Vm3	414.2 $\pm$ 1.4	2.57 $\pm$ 0.06	5.58 $\pm$ 0.10	110.0
Vm3-24	401.3 $\pm$ 1.3	2.69 $\pm$ 0.12	6.60 $\pm$ 0.07	105.8
Vm4	449.1 $\pm$ 5.6	2.53 $\pm$ 0.13	2.19 $\pm$ 0.01	113.7
Vm4-24	426.0 $\pm$ 5.6	2.59 $\pm$ 0.03	3.34 $\pm$ 0.08	110.3

Fig. 7. Vermiculites: a) scheme of the 2:1 layer type structure and b) hydrogen yield from methanol water solution after 4 h and 24 + 4 h of irradiation in the presence of Vm photocatalysts related to the negative tetrahedral (T) charge and to the octahedral (O) charge.

Table 5
The yields of elements Na, K, Mg, Ca, Fe and Al released from vermiculites into methanol water.

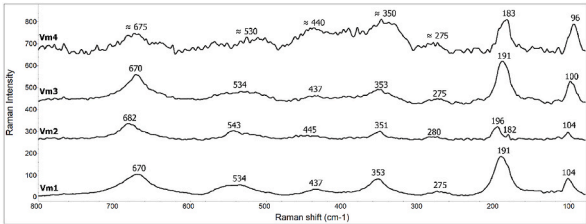| Sample	Na (mg/L)	K (mg/L)	Mg (mg/L)	Ca (mg/L)	Fe (mg/L)	Al (mg/L)
Vm1-24	23.67	<0.01	0.01	0.04	<0.05	<0.02
Vm2-24	2.25	<0.01	1.07	0.68	1.93	0.26
Vm3-24	5.47	<0.01	0.42	0.53	0.26	<0.20
Vm4-24	3.25	0.01	1.58	1.00	<0.05	<0.20

Fig. 8. Raman spectra of raw vermiculites from 800 to 50 cm^{-1}.

vermiculite intermediate structure (Fig. 1).

The other Raman bands (at about 535 cm^{-1}, 440 cm^{-1}, 350 cm^{-1}, and 270 cm^{-1}) are relatively weak and "loaded" by (greater or lesser) level of spectral noise. As has been noted above, only the Raman bands of sample Vm1 spectrum have acceptable level of spectral noise to allow for precise determination of bands wavenumbers. In contrast, the noise in sample Vm4 spectra (due to very significant level of fluorescence) is very high and therefore it was impossible to make an exact determination of wavenumbers of the bands. The bands assignments are as follows: the band at about 540 cm^{-1} (534 cm^{-1} in Vm1 and Vm3; 543 cm^{-1} in Vm2 and about 530 cm^{-1} in Vm4) and the band at about 350 cm^{-1} (353 cm^{-1} in Vm1 and Vm3; 351 cm^{-1} in Vm2; and about 350 cm^{-1} in Vm4) belong to the deformation vibration of O-Mg-O in octahedral sites of vermiculites. The band at about 440 cm^{-1} (437 cm^{-1} in Vm1 and Vm3;

Table 6

The Raman wavenumbers positions in vermiculites (Vm)and vermiculites after 24+4h photocatalytic test (Vm-24) with the assignments of the bands according to the references.

Sample/Wavenumber (cm^{-1})								Assignment	Reference
Vm1	Vm1-24	Vm2	Vm2-24	Vm3	Vm3-24	Vm4	Vm4-24		
670	670	682	686	670	670	675	675	δ Mg-O^O	[38,49–52]
534	534	543	543	534	534	530	530	δ O-Mg-O^O	[38,49–52]
437	437	445	445	437	437	440	440	δ O-Si-O^T	[38,49–52]
–	–	–	392	–	–	–	–	δ O-Mg-O	[55]
353	353	351	351	353	353	350	350	δ O-Mg-O^O	[38,49–52]
275	266	280	280	275	285	275	275	δ Si-O-Si^T	[38,49–52]
–	–	–	235	–	–	–	–	δ O-Mg-O^O	[52]
191	191	196	196	191	191	183	183	δ Mg-O-Mg^O	[38,49–52]
		182	182					δ Mg-O^O	[54]
–	147	–	–	–	–	–	–	δ Si$_2$O$_5^T$	[49,53]
104	104	104	104	100	100	96	96	Cations^I	[38,49–52]

^{O} = Octahedra; ^{T} = Tetrahedra; ^{I} = Interlayer.

445 cm^{-1} in Vm2; and at about 440 cm^{-1} in Vm4) corresponds to the deformation of O–Mg–O in MgO$_6$ polyhedra coupled to O–Si–O. The band at about 275 cm^{-1} (275 cm^{-1} in Vm1 and Vm3; 280 cm^{-1} in Vm2; and at about 275 cm^{-1} in Vm4) originated from deformation vibration of Si-O-Si in tetrahedral sites.

The Raman spectra of the Vm-24 photocatalysts confirm the changes in the vibrations of the tetrahedra (Table 6). The Vm1 and
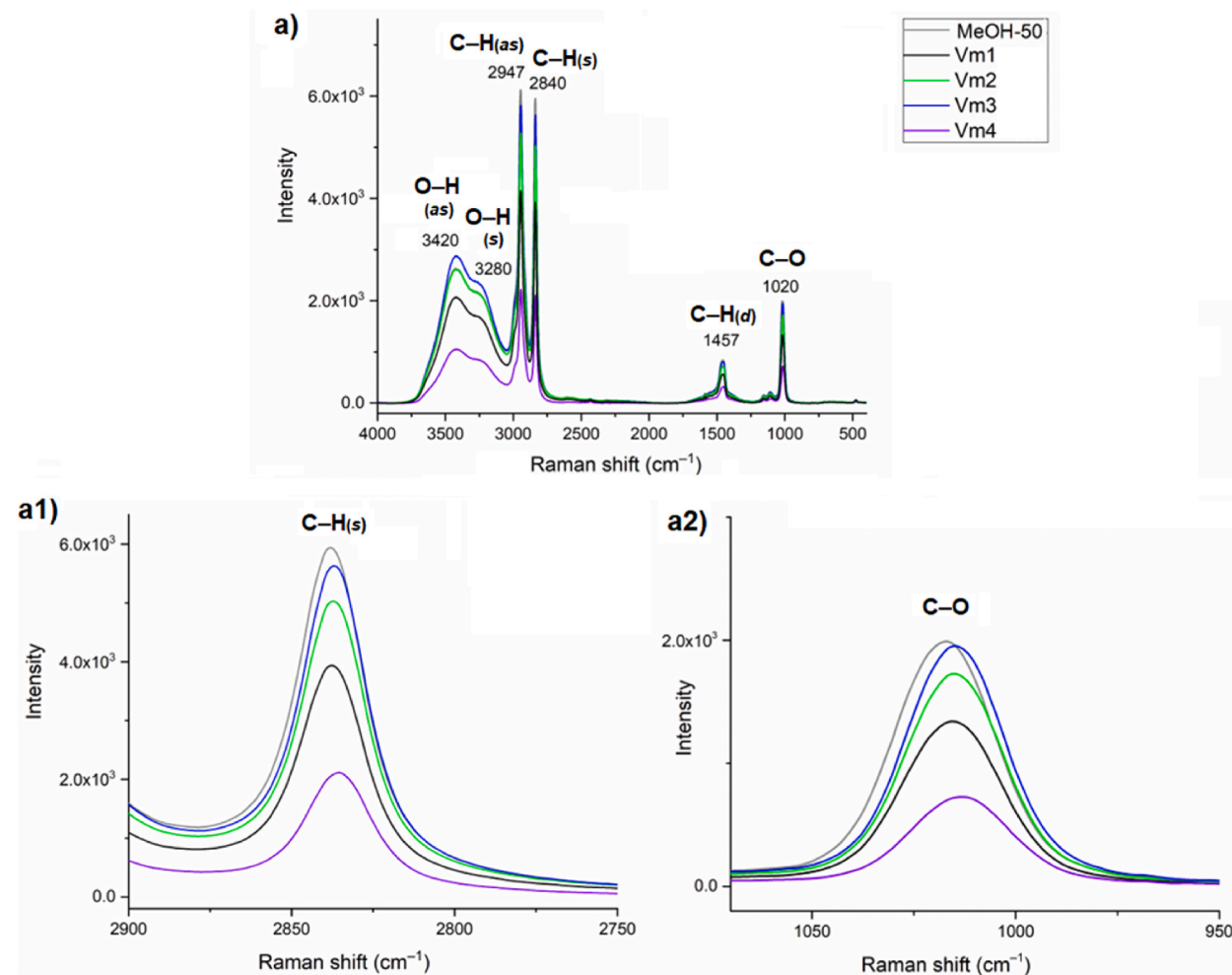

Fig. 9. Raman spectrum of MeOH50 water solution: a) from 4000 cm^{-1} to 400 cm^{-1} in comparison with the Vm-24 photocatalysts presence and the investigated peaks of: a1) C–H$_{(s)}$ band from 2900 to 2750 cm^{-1} and a2) C–O band from 1040 to 1000 cm^{-1}.

Vm1-24 after photocatalytic experiment showed difference only in the band of vibration of Si-O-Si in tetrahedral sites (at about 270 cm^{-1}). This band position was also assigned to the symmetrical stretching of the O-H-O composed of the H proton and two adjacent tetrahedra apical oxygens [54,55]. The shift from band position at 275 cm^{-1} in Vm1 to 266 cm^{-1} in Vm1-24 was very likely caused by the structural changes accompanied by the occurrence of new weak band at 147 cm^{-1}. This band at 147 cm^{-1} was observed in the Raman spectra of several Na-smectites and was assigned to the ring breathing mode of deformation vibration of Si_2O_5 tetrahedra [49, 51].

Some changes are noticeable in the spectra of Vm2 and Vm2-24 after photocatalytic experiment. First, a shift of band wavenumber of deformation vibration (E_3) of Mg-O in octahedral sites of vermiculites (at about 680 cm^{-1}) from 682 cm^{-1} for Vm2 to 686 cm^{-1} for Vm2-24. The change is associated with the appearance of two new bands at 392 cm^{-1} and medium-weak band at 235 cm^{-1}. The band at 392 cm^{-1} was assigned to the Mg-O-Mg deformation vibration of 2:1 layer of chlorites [55]. Similarly, the band at 235 cm^{-1} is related to O-Mg-O deformation vibration of some 2:1 layer clay mineral [21,55].

The Raman spectra of Vm3 samples before and after photocatalytic experiment were very similar (as was the case in the spectra of samples Vm1 and Vm1-24). However, unlike the spectrum of sample Vm1-24, the vibration band of Si-O-Si of tetrahedral sites before photocatalysis at 275 cm^{-1} and after photocatalysis at 285 cm^{-1} was shifted towards higher wavenumbers. This shift with respect to the original Vm1 and Vm4 may be due to the alteration of T–O–T angles or chemical changes in the octahedral sheet. The Raman spectra of the Vm4 samples before and after photocatalytic experiment were too "noisy" to accurately determine the wavenumbers of the characteristic spectral bands. Even so, no wavenumber shift of bands was noted.

3.4.2. Raman spectra of MeOH50

Raman spectra of MeOH shows the bands of water in the range from 3000 to 3800 cm^{-1} (Fig. 9). The band at about 3420 cm^{-1} was assigned to the O–H stretching vibration of water and a band at 3420 cm^{-1} to the O–H stretching vibration of water molecules connected by polymeric hydrogen bonds [56,57] (Fig. 9a). The methanol molecule (CH_3OH) consists of a non-polar methyl group (CH_3-) and polar hydroxyl group (–OH) which can rearrange the structure of water molecules through hydrogen bonding. One water molecule can form up to four hydrogen bonds (two as proton acceptors through the lone-pair electrons on oxygen atom and two as proton donors through two hydrogen atoms). Significant vibrational bands of methanol are bands of C–H bonds (manifesting on the CH_3 asymmetric stretching vibration; 2947 cm^{-1} and CH_3 symmetric stretching vibration; 2840 cm^{-1} and CH_3 asymmetric deformation vibration; 1457 cm^{-1}) and the C-O stretching vibration at 1020 cm^{-1} [58]. Variation of the C–H and C–O stretch frequencies as a function of methanol concentration in water and interaction mainly by hydrogen bonding were studied in a detail over the whole concentration range [59]. Tomza et al. [60] demonstrated maximum heterogeneous cluster of methanol-water complex in the methanol water solution at the molar fraction of methanol 0.5. Yang et al. [30] found that the C–O stretching vibration mode of methanol at the 50 % volume fraction of methanol showed a significant blue shift while the C–H symmetric and asymmetric stretching vibration modes exhibited red shift, indicating no hydrogen bond formed between the CH_3 group of methanol and water molecules. The red shift of the C–H (symmetric and asymmetric) stretching vibrations (Fig. 9a1) may be caused by the cooperative effect of C–O bond (Fig. 9a2) [30]. Interactions between water molecules and methanol result in substantial orientation of the weakly hydrogen-bonded water molecules in the interfacial region. Xiao et al. [31] investigated the competitive adsorption between water molecules and methanol on the surface of the photocatalyst inhibiting the access of methanol to the photocatalyst resulting in decreased hydrogen production.

The Raman spectrum of the MeOH50 after 24 h + 4h photocatalytic experiment with the presence of Vm-24 photocatalysts (Fig. 9) involved the O–H bands of water at 3280 and 3420 cm^{-1} and also involved the bands at 2947 cm^{-1} and at 2840 cm^{-1} assigned to the C–H asymmetric ($C-H_{(as)}$) and C–H symmetric ($C-H_{(s)}$) stretching, the band at about 1457 cm^{-1} assigned to the C–H deformation ($C-H_{(d)}$) and the band at about 1020 cm^{-1} assigned to the C–O stretching (Fig. 9a). In this work, we focused on the stretching vibrations of $C-H_{(s)}$ and C–O (Fig. 9a1 and Fig. 9a2). The frequency of the C-O band at about 1020 cm^{-1} in MeOH50 is much smaller than those in pure methanol at 1033 cm^{-1} (not presented here) and the wavenumber shift can be attributed to the hydrogen bonds between the oxygen pairs of methanol and water protons [30].

Raman spectra of the MeOH50 water solution after 24 h of irradiation and 4 h experiment (Fig. 10) show the C–O band and the $C-H_{(s)}$ band redshift indicating decrease of the methanol content (Fig. 10a). The redshifts of the C–O and C–H bands correspond to the $O-H_{(s)}/C-H_{(s)}$ bands intensity ratio (Fig. 10b and c) and related to the methanol decrease while producing hydrogen yield.

4. Conclusions

This study explored characterizing raw vermiculites with varying chemical compositions defining their crystal chemical formulas expressing the occupation of elements in the structural tetrahedra and octahedra 2:1 layer and interlayer.

The photoluminescence spectra of vermiculites revealed band gap energy charge photoinduced from the electron recombination at the $SiO_4^{4-}/AlO_4^{5-}/FeO_4^{5-}$ tetrahedral centers corresponding to the semiconductors with the expected photocatalytic efficiency on methanol water degradation to the hydrogen and by-products CO and CH_4.

Among the tested samples, vermiculites Vm1 and Vm4 exhibited the highest hydrogen yields after 4 h of UV irradiation, while the intermediate chlorite-vermiculite structure (Vm2) showed lower photocatalytic activity. In addition, it was found that the activity of vermiculite samples decreases over time due to release of cations from crystalline structure into the methanol solution this depends on variable chemistry of the structure building units. In comparison, this was not observed in case of TiO_2 Evonik P25. However, it is important to mention, that P25 is specifically prepared photocatalyst, but vermiculites are natural minerals without any modification.

The Raman spectra confirmed a decrease in methanol content after extended irradiation, indicated by redshifts in C-H and C-O band
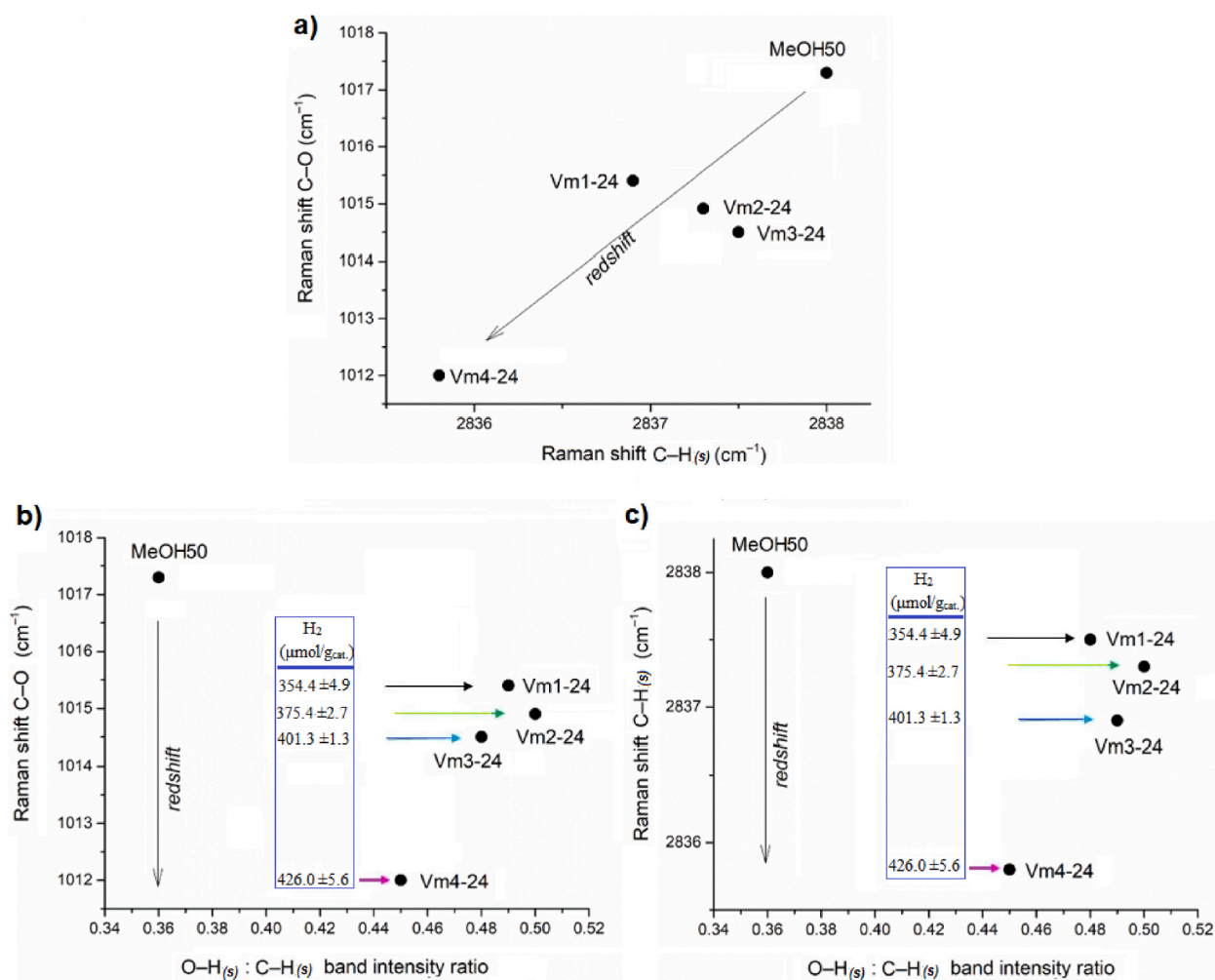
Fig. 10. MeOH50 water solution in the presence of vermiculites after 24 h irradiation and 4 h experiment according to the Raman bands shifts: a) C–O vs. C–H$_{(s)}$; b) C–O vs O–H$_{(s)}$: C–H$_{(s)}$ band intensity ratio and c) C–H$_{(s)}$ vs O–H$_{(s)}$: C–H$_{(s)}$ band intensity ratio. In the box is the yield of hydrogen in the presence of each vermiculite (Table 4).

vibrations. These changes were associated with the production of hydrogen, further supporting the catalytic role of vermiculite in methanol decomposition and proving hydrogen is not formed from photocatalytic water splitting.

In summary, the study suggests that vermiculites, especially those with high negative layer charges originated from tetrahedra, could serve as effective, environmentally friendly photocatalysts for hydrogen production from methanol-water mixtures. This highlights their potential application in clean energy generation and environmental remediation.

CRediT authorship contribution statement

Marta Valášková: Writing – review & editing, Writing – original draft, Validation, Methodology, Formal analysis, Conceptualization. **Miroslava Filip Edelmannová:** Visualization, Validation, Investigation, Data curation. **Martin Reli:** Investigation, Methodology, Writing – review & editing. **Michal Ritz:** Writing – review & editing, Methodology, Investigation, Formal analysis. **Alexandr Martaus:** Methodology, Investigation, Formal analysis. **Eva Plevová:** Software, Methodology. **Kamila Kočí:** Supervision, Methodology, Conceptualization.

Ethical approval

All the authors declare that the manuscript does not have studies on human subjects, human data or tissue, or animals.

Declaration of competing interest

The authors declare that they have no known competing financial interests or personal relationships that could have appeared to influence the work reported in this paper.

Acknowledgements

Appendix A. Supplementary data

Supplementary data to this article can be found online at https://doi.org/10.1016/j.heliyon.2025.e42366.

References

[1] M. Nielsen, E. Alberico, W. Baumann, H.J. Drexler, H. Junge, S. Gladiali, M. Beller, Low-temperature aqueous-phase methanol dehydrogenation to hydrogen and carbon dioxide, Nature 495 (2013) 85–89, https://doi.org/10.1038/nature11891.

[2] R.D. Cortright, R.R. Davda, J.A. Dumesic, Hydrogen from catalytic reforming of biomass-derived hydrocarbons in liquid water, Nature 418 (2002) 964–967, https://doi.org/10.1038/nature01009.

[3] J. Shabaker, R. Davda, G. Huber, R. Cortright, J. Dumesic, Aqueous-phase reforming of methanol and ethylene glycol over alumina-supported platinum catalysts, J. Catal. 215 (2003) 344–352, https://doi.org/10.1016/S0021-9517(03)00032-0.

[4] G. Garcia, E. Arriola, W.-H. Chen, M.D. De Luna, A comprehensive review of hydrogen production from methanol thermochemical conversion for sustainability, Energy 217 (2021) 119384, https://doi.org/10.1016/j.energy.2020.119384.

[5] F. Opoku, K. Govender, C. Sittert, P. Govender, Recent progress in the development of semiconductor-based photocatalyst materials for applications in photocatalytic water splitting and degradation of pollutants, Adv. Sustain. Syst. 1 (2017), https://doi.org/10.1002/adsu.201700006.

[6] C. Belver, J. Bedia, A. Gómez-Avilés, M. Peñas-Garzón, J.J. Rodriguez, Chapter 22 - semiconductor photocatalysis for water purification, in: S. Thomas, D. Pasquini, S.-Y. Leu, D.A. Gopakumar (Eds.), Nanoscale Materials in Water Purification, Elsevier, 2019, pp. 581–651.

[7] D. Zhou, D. Jiang, H. Jing, C. Yin, C. Li, Natural aluminosilicate nanoclay mineral for photocatalytic applications: influence of the surface properties in photocatalysis, Appl. Clay Sci. 249 (2024) 107240, https://doi.org/10.1016/j.clay.2023.107240.

[8] H. Jia, J. Zhao, X. Fan, K. Dilimulati, C. Wang, Photodegradation of phenanthrene on cation-modified clays under visible light, Appl. Catal., B 123–124 (2012) 43–51, https://doi.org/10.1016/j.apcatb.2012.04.017.

[9] M. Wang, H. Shi, H. Shao, K. Lu, H. Wang, Y. Yang, Z. Gong, Y. Zuo, S. Gao, Montmorillonite promoted photodegradation of amlodipine in natural water via formation of surface complexes, Chemosphere 286 (2022) 131641, https://doi.org/10.1016/j.chemosphere.2021.131641.

[10] N. Thomas, D.D. Dionysiou, S.C. Pillai, Heterogeneous Fenton catalysts: a review of recent advances, J. Hazard Mater. 404 (2021) 124082, https://doi.org/10.1016/j.jhazmat.2020.124082.

[11] C. Li, N. Zhu, S. Yang, X. He, S. Zheng, Z. Sun, D.D. Dionysiou, A review of clay based photocatalysts: role of phyllosilicate mineral in interfacial assembly, microstructure control and performance regulation, Chemosphere 273 (2021) 129723, https://doi.org/10.1016/j.chemosphere.2021.129723.

[12] A.D. Purceno, A.P.C. Teixeira, A.B. Souza, J.D. Ardisson, J.P. de Mesquita, R.M. Lago, Ground vermiculite as catalyst for the Fenton reaction, Appl. Clay Sci. 69 (2012) 87–92, https://doi.org/10.1016/j.clay.2012.08.010.

[13] A.J. dos Santos, I. Sirés, A.P.M. Alves, C.A. Martínez-Huitle, E. Brillas, Vermiculite as heterogeneous catalyst in electrochemical Fenton-based processes: application to the oxidation of Ponceau SS dye, Chemosphere 240 (2020) 124838, https://doi.org/10.1016/j.chemosphere.2019.124838.

[14] J.I. Martínez-Costa, J. Rivera-Utrilla, R. Leyva-Ramos, M. Sánchez-Polo, I. Velo-Gala, Individual and simultaneous degradation of antibiotics sulfamethoxazole and trimethoprim by UV and solar radiation in aqueous solution using bentonite and vermiculite as photocatalysts, Appl. Clay Sci. 160 (2018) 217–225, https://doi.org/10.1016/j.clay.2017.12.026.

[15] H.D. Rojas-Mantilla, S.C. Ayala-Duran, R.F. Pupo Nogueira, Modification of a Brazilian natural clay and catalytic activity in heterogeneous photo-Fenton process, Chemosphere 291 (2022) 132966, https://doi.org/10.1016/j.chemosphere.2021.132966.

[16] J. Zhang, T. Liu, R. Chen, X. Liu, Vermiculite as a natural silicate crystal for hydrogen generation from photocatalytic splitting of water under visible light, RSC Adv. 4 (2014) 406–408. https://10.1039/C3RA45301D.

[17] M. Valášková, J. Tokarský, J. Pavlovský, T. Prostějovský, K. Kočí, α-Fe₂O₃ nanoparticles/vermiculite clay material: structural, optical and photocatalytic properties, Materials 12 (2019), https://doi.org/10.3390/ma12111880.

[18] M. Valášková, K. Kočí, J. Madejová, J. Pavlovský, B.T. Barrocas, K. Klemencová, α-Fe₂O₃ nanoparticles/iron-containing vermiculite composites: structural, textural, optical and photocatalytic properties, Minerals 12 (2022), https://doi.org/10.3390/min12050607.

[19] M. Valášková, P. Leštinský, M.F. Edelmannová, J. Madejová, K. Kočí, NiO/vermiculite composites prepared for photocatalytic degradation of methanol-water solution and hydrogen generation, Appl. Clay Sci. 259 (2024) 107509, https://doi.org/10.1016/j.clay.2024.107509.

[20] M. Reli, N. Ambrožová, M. Valášková, M. Edelmannová, L. Čapek, C. Schimpf, M. Motylenko, D. Rafaja, K. Kočí, Photocatalytic water splitting over CeO₂/Fe₂O₃/Ver photocatalysts, Energy Convers. Manag. 238 (2021) 114156, https://doi.org/10.1016/j.enconman.2021.114156.

[21] J.T. Kloprogge, Chapter 6 - Raman spectroscopy of clay minerals, in: W.P. Gates, J.T. Kloprogge, J. Madejová, F. Bergaya (Eds.), Developments in Clay Science, Elsevier, 2017, pp. 150–199.

[22] F. Rull, Structural investigation of water and aqueous solutions by Raman spectroscopy, Pure Appl. Chem. 74 (2002), https://doi.org/10.1351/pac200274101859.

[23] S.N. White, Qualitative and quantitative analysis of CO₂ and CH₄ dissolved in water and seawater using laser Raman spectroscopy, Appl. Spectrosc. 64 (2010) 819–827, https://doi.org/10.1366/000370210791666354.

[24] L.F. Scatena, M.G. Brown, G.L. Richmond, Water at hydrophobic surfaces: weak hydrogen bonding and strong orientation effects, Science 292 (2001) 908–912, https://doi.org/10.1126/science.1059514.

[25] A. Laaksonen, P.G. Kusalik, I.M. Svishchev, Three-dimensional structure in Water–Methanol mixtures, J. Phys. Chem. A 101 (1997) 5910–5918, https://doi.org/10.1021/jp970673c.

[26] I. Pethes, L. Pusztai, L. Temleitner, Evolution of the hydrogen-bonded network in methanol-water mixtures upon cooling, J. Mol. Liq. 386 (2023) 122494, https://doi.org/10.1016/j.molliq.2023.122494.

[27] T. Ebukuro, A. Takami, Y. Oshima, S. Koda, Raman spectroscopic studies on hydrogen bonding in methanol and methanol/water mixtures under high temperature and pressure, J. Supercrit. Fluids 15 (1999) 73–78, https://doi.org/10.1016/S0896-8446(98)00126-0.

[28] I. Bakó, T. Megyes, S. Bálint, T. Grósz, V. Chihaia, Water–methanol mixtures: topology of hydrogen bonded network, Phys. Chem. Chem. Phys. 10 (2008) 5004–5011, https://doi.org/10.1039/B808326F.

[29] F. Li, Z. Men, S. Li, S. Wang, Z. Li, C. Sun, Study of hydrogen bonding in ethanol-water binary solutions by Raman spectroscopy, Spectrochim. Acta, Part A 189 (2018) 621–624, https://doi.org/10.1016/j.saa.2017.08.077.

[30] B. Yang, X. Cao, H. Lang, S. Wang, C. Sun, Study on hydrogen bonding network in aqueous methanol solution by Raman spectroscopy, Spectrochim. Acta, Part A 225 (2020) 117488, https://doi.org/10.1016/j.saa.2019.117488.

[31] M. Xiao, A. Baktash, M. Lyu, G. Zhao, Y. Jin, L. Wang, Unveiling the role of water in heterogeneous photocatalysis of methanol conversion for efficient hydrogen production, Angew. Chem. Int. Ed. 63 (2024) e202402004, https://doi.org/10.1002/anie.202402004.

[32] B.-B. Xu, M. Zhou, R. Zhang, M. Ye, L.-Y. Yang, R. Huang, H.F. Wang, X.L. Wang, Y.-F. Yao, Solvent water controls photocatalytic methanol reforming, J. Phys. Chem. Lett. 11 (2020) 3738–3744, https://doi.org/10.1021/acs.jpclett.0c00972.

[33] H.H. Mohamed, G. Wazan, D.H.A. Besisa, Natural clay minerals as heterojunctions of multi-metal oxides for superior photocatalytic activity, Mater. Sci. Eng. B 286 (2022) 116077, https://doi.org/10.1016/j.mseb.2022.116077.

[34] H.A.O. Macedo, M.E.S. Della Giustina, C.G. de Oliveira, I.F. Praxedes, The São Luís de Montes Belos vermiculite deposit, central Brazil: Hydrothermal mineralization associated with intracontinental strike slip zones, J. South. Am. Earth. Sci. 88 (2018) 459–479, https://doi.org/10.1016/j.jsames.2018.08.012.

[35] R. Badreddine, F. Grandjean, D. Vandormael, A.M. Fransolet, G.J. Long, An ^{57}Fe Mössbauer spectral study of vermiculitization in the Palabora Complex, Republic of South Africa, Clay Miner. 35 (2000) 653–663, https://doi.org/10.1180/000985500547115.

[36] A. Wiewióra, E. Dubińska, Origin of minerals with intermediate chlorite-vermiculite structure (Szklary, Poland), Chem. Geol. 60 (1987) 185–197, https://doi.org/10.1016/0009-2541(87)90124-0.

[37] M.D. Foster, Interpretation of the Composition and a Classification of the Chlorites, Professional Paper, 1962.

[38] A.C. Prieto, J.M. Lobón, J.M. Alía, F. Rull, F. Martin, Thermal and spectroscopic analysis of natural trioctahedral chlorites, J. Therm. Anal. 37 (1991) 969–981, https://doi.org/10.1007/BF01932795.

[39] P. Makuła, M. Pacia, W. Macyk, How to correctly determine the band gap energy of modified semiconductor photocatalysts based on UV–vis spectra, J. Phys. Chem. Lett. 9 (2018) 6814–6817, https://doi.org/10.1021/acs.jpclett.8b02892.

[40] J. Tauc, R. Grigorovici, A. Vancu, Optical properties and electronic structure of amorphous germanium, Phys. Status Solidi B 15 (1966) 627–637, https://doi.org/10.1002/pssb.19660150224.

[41] S. Phanichphant, A. Nakaruk, K. Chansaenpak, D. Channei, Evaluating the photocatalytic efficiency of the BiVO$_4$/rGO photocatalyst, Sci. Rep. 9 (2019) 16091, https://doi.org/10.1038/s41598-019-52589-5.

[42] G. Žerjav, K. Žižek, J. Zavašnik, A. Pintar, Brookite vs. rutile vs. anatase: what's behind their various photocatalytic activities? J. Environ. Chem. Eng. 10 (2022) 107722 https://doi.org/10.1016/j.jece.2022.107722.

[43] K. Somaiah, M. Venkatanarayana, B. Sathyanarayana, Thermally stimulated luminescence of montmorillonite clay, Cryst. Res. Technol. 26 (1991) 357–362, https://doi.org/10.1002/crat.2170260320.

[44] M.A. Mahadik, S.S. Shinde, V.S. Mohite, S.S. Kumbhar, K.Y. Rajpure, A.V. Moholkar, C.H. Bhosale, Photoelectrocatalytic activity of ferric oxide nanocatalyst: a synergestic effect of thickness, Ceram. Int. 40 (2014) 9463–9471, https://doi.org/10.1016/j.ceramint.2014.02.019.

[45] M.A. Gondal, A. Hameed, Z.H. Yamani, Hydrogen generation by laser transformation of methanol using n-type WO$_3$ semiconductor catalyst, J. Mol. Catal. Chem. 222 (2004) 259–264, https://doi.org/10.1016/j.molcata.2004.08.022.

[46] W. Guo, T. Guo, Y. Zhang, L. Yin, Y. Dai, Progress on simultaneous photocatalytic degradation of pollutants and production of clean energy: a review, Chemosphere 339 (2023) 139486, https://doi.org/10.1016/j.chemosphere.2023.139486.

[47] R.A. Schoonheydt, Reflections on the material science of clay minerals, Appl. Clay Sci. 131 (2016) 107–112, https://doi.org/10.1016/j.clay.2015.12.005.

[48] F. Brandt, D. Bosbach, E. Krawczyk-Bärsch, T. Arnold, G. Bernhard, Chlorite dissolution in the acid ph-range: a combined microscopic and macroscopic approach, Geochem. Cosmochim. Acta 67 (2003) 1451–1461, https://doi.org/10.1016/S0016-7037(02)01293-0.

[49] R.L. Frost, L. Rintoul, Lattice vibrations of montmorillonite: an FT Raman and X-ray diffraction study, Appl. Clay Sci. 11 (1996) 171–183, https://doi.org/10.1016/S0169-1317(96)00017-8.

[50] M. Arab, D. Bougeard, K.S. Smirnov, Experimental and computer simulation study of the vibrational spectra of vermiculite, Phys. Chem. Chem. Phys. 4 (2002) 1957–1963, https://doi.org/10.1039/B110768B.

[51] C. Rinaudo, M. Roz, V. Boero, M. Franchini-Angela, FT-Raman spectroscopy on several di- and trioctahedral T-O-T phyllosilicates, Neu. Jb. Mineral., Mh 2004 (2004) 537–554, https://doi.org/10.1127/0028-3649/2004/2004-0537.

[52] M. Ritz, J. Zdrálková, M. Valášková, Vibrational spectroscopy of acid treated vermiculites, Vib. Spectrosc. 70 (2014) 63–69, https://doi.org/10.1016/j.vibspec.2013.11.007.

[53] M. Ritz, M. Valášková, Infrared and Raman spectroscopy of three commercial vermiculites doped with cerium dioxide nanoparticles, Spectrochim. Acta, Part A 201 (2018) 39–45, https://doi.org/10.1016/j.saa.2018.04.053.

[54] A. Tlili, D.C. Smith, J.M. Beny, H. Boyer, A Raman microprobe study of natural micas, Mineral. Mag. 53 (1989) 165–179, https://doi.org/10.1180/minmag.1989.053.370.04.

[55] G. Ulian, D. Moro, G. Valdrè, Infrared and Raman spectroscopic features of clinochlore Mg$_6$Si$_4$O$_{10}$(OH)$_8$: a density functional theory contribution, Appl. Clay Sci. 197 (2020) 105779, https://doi.org/10.1016/j.clay.2020.105779.

[56] F. Li, Y. Wang, Z. Li, Z. Men, C. Sun, Enhanced stimulated Raman scattering by a pressure-controlled shock wave in liquid water, J. Phys. Chem. Lett. 10 (2019) 4812–4816, https://doi.org/10.1021/acs.jpclett.9b01956.

[57] P.A. Giguère, Bifurcated hydrogen bonds in water, J. Raman Spectrosc. 15 (1984) 354–359, https://doi.org/10.1002/jrs.1250150513.

[58] J. Pal, A. Patla, R. Subramanian, Thermodynamic properties of forming methanol-water and ethanol-water clusters at various temperatures and pressures and implications for atmospheric chemistry: a DFT study, Chemosphere 272 (2021) 129846, https://doi.org/10.1016/j.chemosphere.2021.129846.

[59] S. Dixit, W.C.K. Poon, J. Crain, S. Dixit, W.C.K. Poon, Hydration of methanol in aqueous solutions: a Raman spectroscopic study, J. Phys. Condens. Matter 12 (2000) L323, https://doi.org/10.1088/0953-8984/12/21/103.

[60] P. Tomza, W. Wrzeszcz, S. Mazurek, R. Szostak, M.A. Czarnecki, Microheterogeneity in binary mixtures of water with CH$_3$OH and CD$_3$OH: ATR-IR spectroscopic, chemometric and DFT studies, Spectrochimica acta. Part A, Molecular and biomolecular spectroscopy 197 (2018) 88–94, https://doi.org/10.1016/j.saa.2018.01.068.